Angle- and Energy-Resolved Plasmon Coupling in Gold Nanorod Dimers

Lei Shao,† Kat Choi Woo,† Huanjun Chen, Zhao Jin, Jianfang Wang,* and Hai-Qing Lin*

Department of Physics, The Chinese University of Hong Kong, Shatin, Hong Kong SAR, China. †These authors contributed equally to this work.

ARTICLE

ABSTRACT The plasmon coupling in the dimers of Au nanorods linked together at their ends with dithiol molecules has been studied. The plasmon coupling in the dimers composed of similarly sized nanorods gives antibonding and bonding plasmon modes. The plasmon wavelengths of the two modes have been found to remain approximately unchanged, with the scattering intensity ratio between the antibonding and bonding modes decaying rapidly as the angle between the nanorods is increased. This plasmon coupling behavior agrees with that obtained from both electrodynamic calculations and modeling on the basis of the dipole—dipole interaction. The electric field in the gap region is largely enhanced for the bonding mode, while that for the antibonding mode is even smaller than the far field, highlighting the importance of selecting appropriate plasmon modes for plasmon-enhanced spectroscopies. An anti-crossing-like behavior in the plasmon coupling energy diagram has further been revealed for linearly end-to-end assembled dimers composed of differently sized nanorods. This result will be useful for plasmonic applications where the plasmon wavelength is required to be controllable but without sacrificing the electric field enhancement.

KEYWORDS: assembly · dithiol · gold nanorods · plasmon coupling · scattering

Noble metal nanocrystals exhibit rich plasmonic properties. When metal nanocrystals are placed adjacent to each other, their localized surface plasmons are coupled together. The local electric field enhancement in the gap region of plasmon-coupled metal nanocrystals is usually much larger than that associated with isolated nanocrystals. The plasmon coupling between noble metal nanocrystals has therefore been employed for enhancing optical signals, including Raman,[1,2] second-harmonic,[3] fluorescence,[4] and two-photon photoluminescence,[5] and applied in photolithography,[6] two-photon polymerization,[7] and nanometric optical tweezers.[8] Because of the plasmon coupling-induced large electric field enhancement, closely spaced metallic nanorods[9,10] can function as optical nanoantennas to link propagating radiation with confined optical fields. In addition, plasmon-coupled metal nanocrystal chains can act as subwavelength waveguides in integrated photonic circuits.[11,12] Moreover, the plasmon coupling among metal nanocrystals is usually accompanied with large shifts in their extinction or scattering spectral peaks, which are often accompanied with distinct color changes. Such plasmon coupling-induced color changes have been taken as the basis for the development of many chemical and biological sensing methods.[13,14]

A number of experiments and electrodynamic calculations have been performed on the plasmon coupling.[15] These studies have mainly focused on the dependence of the coupling strength on the spacing between metal nanocrystals that have different shapes, such as nanospheres,[16−23] nanodisks,[24,25] nanoshells,[26,27] and nanorods.[28−34] Both experiments and calculations show that the coupling-induced plasmon shift of metal nanocrystal dimers decays nearly exponentially with the interparticle spacing.[21,25] If both the plasmon shift and the interparticle spacing are normalized against the plasmon wavelength and characteristic size of the isolated nanocrystal, respectively, the decay length is found to be constant, irrespective of the nanocrystal size, shape, metal type, and medium dielectric constant. Because noble metal nanocrystals do not blink or bleach, the universal scaling behavior of the plasmon coupling in metal nanocrystal dimers has been utilized to measure and monitor dynamic distance changes between biological macromolecules over a length range of 1−100 nm,[35−37] which is larger than the upper limit of 10 nm set by Förster resonance energy transfer.

Noble metal nanorods exhibit transverse and longitudinal plasmon resonance modes that correspond to the electron

*Address correspondence to jfwang@phy.cuhk.edu.hk, hqlin@phy.cuhk.edu.hk.

Received for review January 29, 2010 and accepted May 11, 2010.

Published online May 18, 2010. 10.1021/nn100180d

oscillations perpendicular and parallel to the length axis, respectively. The resonant excitation and scattering of the longitudinal plasmon mode of metal nanorods are inherently polarized along the length axis. The plasmon coupling between metal nanorods is therefore expected to be highly dependent not only on their interparticle spacing but also on their relative orientation. Up to date, the spacing-dependent plasmon coupling between side-by-side and linearly end-to-end aligned metal nanorods have been well-investigated.[28−33] The importance of the nanorod orientation on the plasmon coupling has been pointed out in a few recent experiments,[31−34] but the dependence of the plasmon coupling on the inter-rod angle has rarely been explored. Here we report a systematic study of the plasmon coupling in Au nanorod dimers as a function of the relative orientation between the two nanorods. The nanorods are connected covalently at their ends through dithiol molecules and form varying angles between them. Two plasmon modes, which arise from the plasmon hybridization and correspond to antibonding and bonding modes, are observed in the dimers composed of similarly sized nanorods. Their scattering peak wavelengths are found to fluctuate around their respective average values, and the scattering intensity ratio between the two modes is seen to decay rapidly with the nanorod angle. This experimental decay is in agreement with that found from electrodynamic calculations and a dipolar model. Moreover, an anti-crossing-like behavior in the plasmon coupling energy diagram is revealed for linearly end-to-end connected nanorod dimers from an unprecedented experimental study of the dependence of the coupled plasmon energy on the plasmon energies of the nanorod monomers. These results will be highly useful for plasmon-enhanced spectroscopies. The energy-resolved plasmon coupling suggests that the coupled plasmon energy can be controlled by varying the plasmon energies of isolated metal nanocrystals instead of changing the spacing between nanocrystals. The latter is undesirable because an increase in the spacing will dramatically reduce the local electric field enhancement. The angle-dependent coupling indicates that large electric field enhancements occur only under the excitation of the bonding plasmon mode. In contrast, the local electric field in the gap region is reduced when metal nanorod dimers are excited at their antibonding mode. In addition, our results will also help in developing plasmon-based optical and optomechanical devices.

RESULTS AND DISCUSSION

The Au nanorods were prepared using a seeded growth method[38] together with anisotropic oxidation.[39,40] All of the nanorod samples in our experiments have the same average diameter but different average lengths. Figure 1a shows the transmission electron microscopy (TEM) image of the nanorod sample used for the angle-resolved study. This nanorod sample has an average diameter, length, and aspect ratio of 32 ± 3 nm, 63 ± 5 nm, and 2.0 ± 0.2, respectively, with a longitudinal plasmon resonance wavelength (LPRW) of 618 nm in aqueous solutions. The nanorod assembly was realized by first dispersing the nanorods in a mixture of H_2O and CH_3CN and then adding 1,8-octanedithiol as a linking molecule.[41] The assembly process in the mixture solvent was monitored spectrally (Figure S1, Supporting Information). The assembled nanorods were deposited on conductive indium tin oxide (ITO)-coated glass substrates. Figure 1b−d shows the TEM images of three representative dimers composed of the similarly sized nanorods. The two nanorods in each dimer are connected at the ends through the dithiol molecules and form different angles. The spacing between the two nanorods was estimated from high-resolution TEM imaging to be ~1 nm (Figure 1e). This value is smaller than the molecular length of the dithiol, which is estimated to be ~1.2 nm, because the carbon chain of the dithiol is flexible. The chain flexibility is also consistent with the formation of the nanorod dimers with varying nanorod angles.[41]

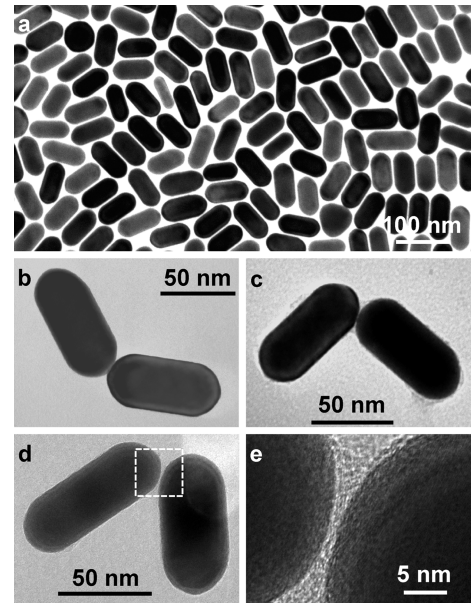

Figure 1. (a) TEM image of the Au nanorods. (b−d) TEM images of three nanorod dimers. The angles between the two nanorods are 128, 97, and 58°, respectively. (e) High-resolution TEM image of the area indicated with a dashed box in (d), showing the presence of a gap between the two nanorods.

The scattering properties of the nanorod dimers were measured using the dark-field technique. A pattern-matching method[42] was utilized to locate the same dimers on their scattering and scanning electron microscopy (SEM) images so that the scattering spectrum of each dimer could be correlated with its geometrical structure (Figure S2, Supporting Information). Figure 2a−d shows the scattering spectra and corresponding SEM images of four representative nanorod

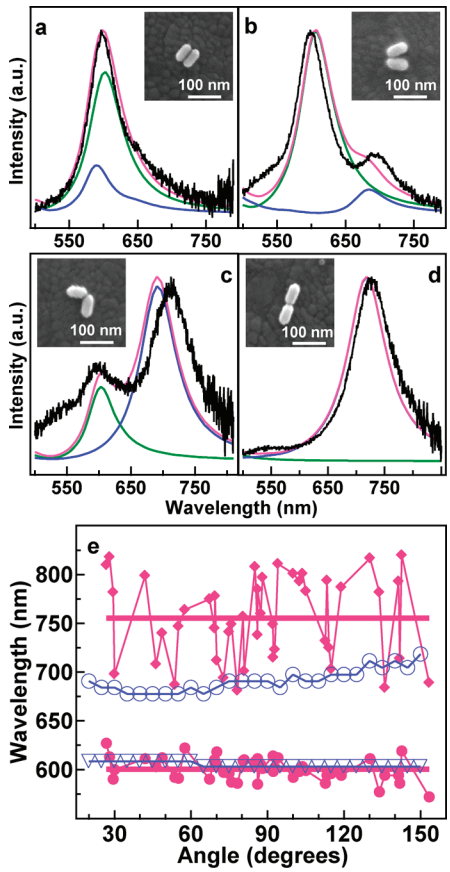

Figure 2. (a−d) Scattering spectra and SEM images (insets) of four nanorod dimers at angles of 0, 30, 87, and 180°, respectively. The black curves are the experimental scattering spectra. The colored curves are the scattering spectra obtained from the FDTD calculations at the nanorod angles of 0, 30, 90, and 180°, respectively. The green and blue curves represent the antibonding and bonding modes. The pink curves are the sums of the green and blue curves. (e) Peak wavelengths of both the antibonding (lower) and bonding (upper) modes *versus* the nanorod angle. The pink symbols denote the data from the experiments, with the horizontal lines representing the average values. The blue symbols represent the data obtained from the FDTD calculations at every 5°.

dimers at angles of 0, 30, 87, and 180°, respectively. When the angle between the two nanorods in the dimer is 0 and 180°, only one scattering peak is seen. When the angle is between ~30 and ~150°, two scattering peaks are observed.

We measured the scattering spectra of 45 nanorod dimers that have the nanorod angle varying between 30 and 150°. The two scattering peak wavelengths are plotted as a function of the nanorod angle measured from the SEM imaging (Figure 2e). The two scattering peaks are seen to fluctuate around their respective average values at 600 and 755 nm. A gap is clearly visible between the lower- and higher-energy branches. The fractional standard deviations of the lower- and higher-energy branches are 6 and 2% in terms of energy, respectively. Moreover, as the nanorod angle is increased, the higher-energy peak becomes weaker, while the lower-energy one becomes stronger. When the ratio between the two scattering peak intensities is plotted as a function of the nanorod angle, it is found to decay rapidly with the nanorod angle (Figure 3a). This relationship between the scattering property of metal nanorod dimers and the nanorod angle has not been observed before. It could form the basis of nanoscale protractors to measure angles in nanoscale devices and biological entities. We point out here that only the data points for the dimers composed of the nanorods that have similar sizes under the SEM imaging are included in the plots shown in Figures 2e and 3a. Those dimers that contain clearly shorter or longer nanorods have been excluded. However, small variations in the nanorod diameter and length are unavoidable. Their presence, together with the small change in the spacing between the nanorods due to the flexible chain of the dithiol, causes the fluctuation in the scattering peak wavelengths. In addition, a control experiment was performed, where the nanorod dimers deposited on the ITO substrates were thermally treated at 200 °C for 90

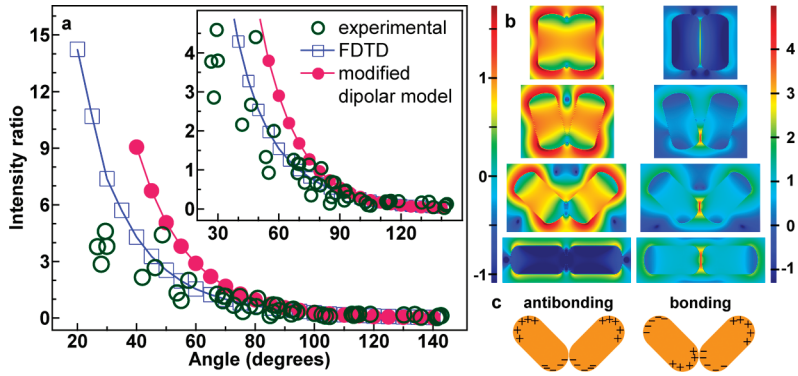

Figure 3. (a) Plot of the intensity ratio between the scattering peaks of the antibonding and bonding modes *versus* the nanorod angle in the dimer. The green, blue, and pink symbols represent the data obtained from the experiments, FDTD calculations, and modified dipolar model, respectively. The inset shows the enlarged plot. (b) Electric field intensity enhancement contours obtained from the FDTD calculations for the nanorod dimers at 0, 30, 90, and 180°, respectively. The left and right contours are for the antibonding and bonding modes. The contours were calculated at their respective plasmon peak wavelengths. The enhancement is drawn at the logarithmic scale. (c) Schematic description of the charge distributions associated with the antibonding and bonding modes in the nanorod dimer at 90°. The charge distributions are derived from the field intensity enhancement contours.

min with a ramp rate of 3 °C/min. The thermal treatment induces clear and large changes in the scattering spectra of the dimers, but the scattering spectra of the monomers remain unchanged (Figure S3, Supporting Information). The scattering spectral changes suggest that a gap is existent between the nanorods and that the nanorods are welded together to form conductive contacts after the thermal treatment.[24,42]

Finite-difference time-domain (FDTD) calculations were carried out to understand the unprecedented dependence of the plasmonic properties of the nanorod dimers on the nanorod angle. The calculations were first performed for the longitudinal plasmon mode of the nanorod monomer to extract the necessary dimensional and dielectric parameters because this plasmon mode was readily observed experimentally. The dielectric function of gold is expressed according to the Drude model in conjunction with the surface damping by

$$\varepsilon(\omega) = \varepsilon_\infty - \frac{\omega_p^2}{\omega^2 + i\gamma\omega} \quad (1)$$

where $\varepsilon_\infty = 9.5$ is the high-frequency contribution to the dielectric function, $\hbar\omega_p = 8.96$ eV is the bulk plasma frequency of gold, and γ is the damping constant. The scattering peak width of the nanorod monomer is mainly determined by the damping constant; $\hbar\gamma$ is found to be 0.144 eV by comparing the calculated peak width with the experimental one. The measured scattering peak wavelengths of the nanorod monomers are averaged at 619 nm, which is equal to the calculated peak wavelength (Figure S4, Supporting Information). The calculated scattering peak is in very good agreement with the experimental ones in terms of both the width and peak position. The above dielectric parameters were therefore employed for all of the calculations and modeling throughout this work.

The in-plane plasmon modes of the nanorod dimers were considered during the FDTD calculations by assuming that the excitation light is polarized within the substrate plane either along or perpendicular to the bisector of the nanorod angle. Under this assumption, according to the plasmon hybridization model,[17,29] there will be four hybridized plasmon modes because each nanorod monomer has a transverse and longitudinal plasmon modes. When the nanorod angle in the dimer is equal to 0 and 180°, corresponding to the side-by-side and end-to-end orientations, the transverse and longitudinal modes are hybridized separately to give the bonding and antibonding modes (Figure S5, Supporting Information). Two of them are optically active, and the other two are dark modes. The FDTD calculations indicate that, at 0°, the scattering peaks arising from the optically active longitudinal antibonding and transverse bonding modes are close to each other (Figures 2a and 3b). Their sum appears as one single peak at 598 nm, which is in agreement with the experimental one. At 180°, the transverse antibonding and longitudinal bonding modes are optically active, but the former is very weak. Therefore, only one peak is observed experimentally (Figures 2d and 3b).

The FDTD calculations show two scattering peaks when the nanorod angle is in the range from 15 to 160°. The higher-energy mode is excited when the excitation polarization is parallel to the bisector, while the lower-energy one is excited when the excitation polarization is perpendicular to the bisector (Figure 2b,c and Figure S6, Supporting Information). Due to the reduction in the symmetry of the nanorod dimer, these two modes cannot be simply ascribed to the separate hybridization of the transverse and longitudinal modes of the monomer. The transverse and longitudinal modes are instead mixed together to give new plasmon modes. They are generally known as antibonding and bonding modes.[29] Although the transverse and longitudinal modes are mixed together due to the symmetry reduction, the calculated charge distributions (Figure 3c) show that the hybridized modes are essentially contributed by the longitudinal dipolar modes of the individual nanorods. The calculated peak wavelengths of the antibonding and bonding modes are seen to remain nearly constant (Figure 2e). The deviation of the calculated wavelengths from the measured ones can be ascribed to the use of a spacing of 1.0 nm between the two nanorods, which is twice the mesh size. The actual spacing might be slightly smaller than 1.0 nm. The calculated intensity ratio between the two modes is also found to decay rapidly with the nanorod angle, which is in good agreement with the experimental result (Figure 3a). The observation of only two hybridized plasmon modes is probably due to the other two modes being either too weak or out of the wavelength range of our optical system. The calculated scattering intensities in the wavelength range shorter than ~550 nm are also inaccurate because of the use of the Drude model, which neglects the interband transitions. In addition, there must be transitions from the bonding mode to the purely transverse bonding mode when the nanorod angle becomes close to 0° and from the antibonding mode to the purely transverse antibonding mode when the nanorod angle becomes 180°. These transitions are currently elusive both experimentally and computationally.

One interesting aspect about the antibonding and bonding modes of the nanorod dimers is their distinct electric fields in the gap region. When the nanorod dimers are excited resonantly at their bonding mode, the electric field in the gap region is largely enhanced, forming so-called "hot spots". This field enhancement has been well-known for plasmon-coupled metal nanostructures. In contrast, when the nanorod dimers are excited resonantly at their antibonding mode, the electric field in the gap region is reduced in comparison to

the far field (Figure 3b and Figure S7, Supporting Information). The gap region between the nanorods can therefore be thought of as "cold spots" because of the electric field reduction. This result is very important for plasmon-enhanced spectroscopies on elongated metal nanocrystal assemblies because the gap regions between elongated metal nanocrystals do not always form hot spots even under resonant excitation. Optical signal enhancements can only be achieved by exciting the bonding plasmon mode.

We further developed a dipolar model in order to have an underlying picture of the angle-dependent plasmonic behavior of the nanorod dimers. Because the nanorods are much smaller than the wavelength of the scattered light, only the dipolar contribution is considered. The model is therefore based on the electrostatic interaction between the two point electric dipoles situated at the centers of the two nanorods. The validity of the dipole approximation is corroborated from the FDTD calculations by summing the electric dipole moment at each grid point according to

$$\mathbf{p}_i = (\varepsilon - 1)\varepsilon_0 \sum_j \mathbf{E}_{\mathrm{loc},j} \tag{2}$$

where ε is the dielectric function of gold, ε_0 is the vacuum permittivity, $\mathbf{E}_{\mathrm{loc},j}$ represents the local electric field at the grid point j, and i is B and A, for the bonding and antibonding plasmon modes, respectively. The scattering peak intensity ratio between the antibonding and bonding modes can be calculated according to

$$\eta = \left(\frac{\lambda_B}{\lambda_A}\right)^4 \left|\frac{p_A}{p_B}\right|^2 \tag{3}$$

where p_A and p_B are calculated at the scattering peak wavelengths λ_A and λ_B of the two modes, respectively. The resultant plot of the scattering intensity ratio *versus* the nanorod angle agrees reasonably well with that directly obtained from the FDTD-calculated scattering spectra (Figure S8, Supporting Information), suggesting that the scattering from the nanorod dimers is dominantly contributed by the dipole radiation.

In the dipolar model, the nanorod monomer is treated as a prolate spheroid with a semimajor axis of $a = 32$ nm and a semiminor axis of $b = 16$ nm.[43] In the quasi-static regime, the electric polarizabilities corresponding to the longitudinal and transverse plasmon modes can be written according to the Clausius−Mossotti equation as[44]

$$\alpha_j = \frac{4\pi ab^2}{3P_j} \frac{\varepsilon - \varepsilon_m}{\varepsilon + \left(\frac{1 - P_j}{P_j}\right)\varepsilon_m} \tag{4}$$

where ε_m is the dielectric constant of the surrounding medium, and j is L or T, for the longitudinal and transverse modes, respectively; ε_m is set at 1.45[2] to take into account the ITO substrate. P_L and P_T are the depolarization factors and can be expressed by

$$P_L = \frac{1 - e^2}{e^2}\left[\frac{1}{2e}\ln\left(\frac{1 + e}{1 - e}\right) - 1\right] \tag{5}$$

$$P_T = (1 - P_L)/2 \tag{6}$$

$$e = \sqrt{1 - \left(\frac{b}{a}\right)^2} \tag{7}$$

After the polarizability is obtained, the scattering cross section as a function of wavelength can be determined according to

$$C_{sca} = \frac{1}{6\pi}\left(\frac{2\pi}{\lambda}\right)^4 |\alpha|^2 \tag{8}$$

The calculated scattering spectrum for the longitudinal plasmon mode of the nanorod monomer shows a peak at 612 nm (Figure S4, Supporting Information), which is close to the experimental one.

The overall electric polarizability $\boldsymbol{\alpha}_i$ ($i = 1,2$) of each nanorod in the dimer can be determined from eq 4. Under an externally applied electric field $\mathbf{E}_0$, the electric dipole moment of each nanorod is given by

$$\mathbf{p}_i = \varepsilon_0 \varepsilon_m \boldsymbol{\alpha}_i \cdot \mathbf{E}_i \tag{9}$$

In eq 9, $\mathbf{E}_i$ is the total electric field acting on the nanorod i. It is a sum of $\mathbf{E}_0$ and the field caused by the electric dipole of the other nanorod. It can be expressed by

$$\mathbf{E}_i = \mathbf{E}_0 + \gamma \frac{3(\mathbf{p}_j \cdot \mathbf{e}_{ji})\mathbf{e}_{ji} - \mathbf{p}_j}{4\pi\varepsilon_0\varepsilon_m d^3},\ j \neq i \tag{10}$$

where d is the center-to-center distance between the two nanorods, $\mathbf{e}_{ji}$ is the unit vector pointing from the center of the nanorod j to the center of the nanorod i, and γ is a coefficient introduced to modify the dipole−dipole interaction. The introduction of the modifying coefficient is to account for the substrate effect, multipolar contribution, finite-size effect, and charge redistribution. The latter three factors usually become considerable as the spacing between metal nanocrystals is very small.[18,31] Because these effects are expected to be different for the two plasmon modes of the dimer system, two coefficients are employed. The center-to-center distance is dependent on the nanorod angle θ according to

$$d = \{2[a^2 + b^2 + (a^2 - b^2)\cos\theta]\}^{1/2} + s + (4a - 2b)\sin\frac{\theta}{2} \tag{11}$$

where $s = 1.0$ nm is the surface-to-surface spacing between the two nanorods at the closest point. From eqs 9 and 10, the scattering cross sections C_B and C_A for the bonding and antibonding modes can be derived as (see Figure S9 and the detailed derivation in the Supporting Information)

$$C_B = \frac{1}{6\pi}\left(\frac{2\pi}{\lambda}\right)^4 \left|\frac{4\pi d^3[2\pi d^3(\alpha_L + \alpha_T) - \alpha_L\alpha_T\gamma_B - 2\pi d^3(\alpha_L - \alpha_T)\cos\theta]}{8\pi^2 d^6 - 3\pi d^3(\alpha_L + \alpha_T)\gamma_B + \alpha_L\alpha_T\gamma_B^2 + \pi\gamma_B d^3(\alpha_L - \alpha_T)\cos\theta}\right|^2 \quad (12)$$

$$C_A = \frac{1}{6\pi}\left(\frac{2\pi}{\lambda}\right)^4 \left|\frac{8\pi d^3[\pi d^3(\alpha_L + \alpha_T) + \alpha_L\alpha_T\gamma_A + \pi d^3(\alpha_L - \alpha_T)\cos\theta]}{8\pi^2 d^6 + 3\pi d^3(\alpha_L + \alpha_T)\gamma_A + \alpha_L\alpha_T\gamma_A^2 - \pi\gamma_A d^3(\alpha_L - \alpha_T)\cos\theta}\right|^2 \quad (13)$$

where γ_B and γ_A are the modifying coefficients for the bonding and antibonding modes, respectively.

The scattering spectra for the two plasmon modes of the dimer system can then be calculated according to eqs 12 and 13 to obtain the scattering peak intensities. The values of γ_B and γ_A that give the best fit to the experimental plot between the scattering intensity ratio and the nanorod angle are found to be 3.3 and 0.3, respectively (Figure 3a). The smaller modifying coefficient for the antibonding mode can be ascribed to that the distance between the two electric dipoles for the antibonding mode is larger than that for the bonding mode (Figure 3c). Although the intensity ratio obtained from the dipolar model increases faster than the experimental one as the nanorod angle is reduced, the overall trend resulting from the modeling is close to the experiment one. The model gives two scattering peaks in the angle range of 40 to 140°. When θ is smaller than 40°, the bonding mode is absent. When θ is larger than 140°, the antibonding mode vanishes. In addition, the scattering spectra obtained from the dipolar model are shifted considerably in comparison to the measured ones (Figure S6, Supporting Information). This result is consistent with the previous finding that the dipolar interaction is ineffective in accurately describing the plasmon shift when the gap between metal nanocrystals is very small.[18] We also calculated the scattering spectra of the nanorod dimers using the unmodified dipolar model, where both γ_B and γ_A were set to be 1 (Figure S6, Supporting Information). The intensity ratio is seen to increase even faster than the modified dipolar model as the nanorod angle is decreased (Figure S8, Supporting Information). This result further suggests the necessity for introducing the modifying coefficients to account for the effects of the multipolar contribution, finite-size, and charge redistribution in the nanorod dimers.

We next studied the energy-dependent plasmon coupling in the dimers in which the two nanorods are linearly end-to-end assembled. Because the LPRW of Au nanorods is approximately a linear function of their aspect ratio,[39,40,43] the longitudinal plasmon energy is controlled by the nanorod aspect ratio. The nanorod samples produced from anisotropic shortening have the same average diameter and varying average lengths.[39,40] In this experiment, the length of one nanorod in the dimer was fixed, while that of the other one was changed. The nanorods of different lengths were mixed and assembled together with the same dithiol. Figure 4a shows the scattering spectra and corresponding SEM images of three representative nanorod dimers. A strong scattering peak above 700 nm is clearly observable for all of these dimers. This strong peak is ascribed to the longitudinal bonding plasmon mode. A close look at the spectra reveals the presence of very weak bumps between 600 and 700 nm. These weak bumps are believed to arise from the longitudinal antibonding mode. When a linearly assembled dimer is composed of two nanorods with different lengths, the mirror symmetry is broken. This symmetry breaking leads to a nonzero net dipole moment for the antibonding mode and thus the appearance of a weak peak at a higher energy on the far-field scattering spectrum.[28]

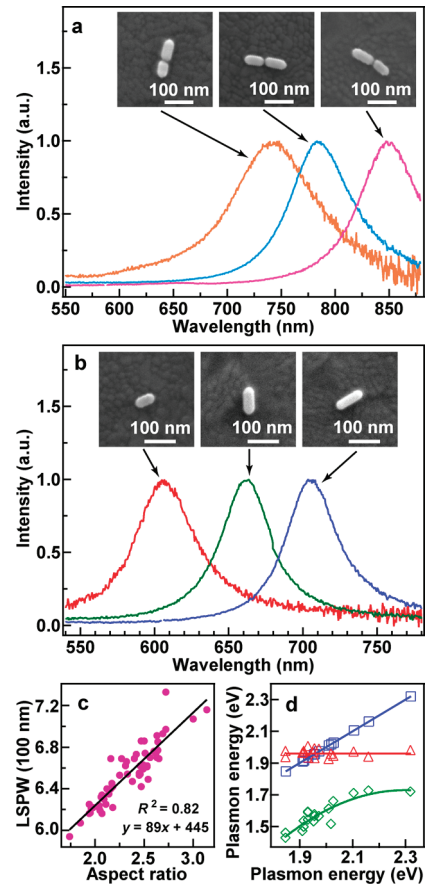

Figure 4. (a) Normalized scattering spectra of three linearly end-to-end assembled dimers composed of the Au nanorods with different lengths. The insets are the SEM images of the corresponding dimers. (b) Normalized scattering spectra of three representative Au nanorods with different LPRWs. The insets show the SEM images of the corresponding nanorods. (c) LPRW *versus* the nanorod aspect ratio. The line is a linear fit. (d) Plasmon coupling energy diagram. The red and blue symbols represent the plasmon energies of the isolated nanorods, and the green symbols represent the coupled plasmon energies of the nanorod dimers. The red line is an average. The blue line is a linear fit. The green line is a fit with a quadratic function to guide the eye.

TABLE 1. Average Sizes and LPRWs of the Elongated Au Nanocrystals and the Coupling-Induced Plasmon Shifts of the Nanocrystal Dimers

nanocrystals	diameter[a] (nm)	length (nm)	$\lambda_{monomer}$[b] (nm)	λ_{dimer}[c] (nm)	$\Delta\lambda$[d] (nm)	$\Delta E/E$[e]
nanorods	32 ± 3	63 ± 5	622 ± 7	805 ± 13	183	(23 ± 2)%
nanobipyramids	32 ± 2	65 ± 3	617 ± 13	813 ± 30	196	(24 ± 3)%
nanobars	44 ± 2	88 ± 5	688 ± 14	854 ± 22	166	(19 ± 3)%

[a]Measured at the middle of the nanocrystals. [b]Represents the LPRW. [c]Coupled plasmon wavelength. [d]$\Delta\lambda = \lambda_{dimer} - \lambda_{monomer}$ is the plasmon shift arising from the plasmon coupling. [e]$\Delta E/E$ is the fractional plasmon shift in terms of energy.

We focus in our experiment on the longitudinal bonding mode of the dimers. The scattering peak wavelengths of the three dimers are measured to be 740, 785, and 850 nm, respectively, for the longitudinal bonding mode.

The scattering spectra of more than 50 nanorod monomers were also recorded in order to find out the dependence of the LPRW on the aspect ratio (Figure 4b). The sizes of the monomers were measured from their SEM images. Figure 4c shows the plot of the LPRW as a function of the aspect ratio, where the aspect ratio ranges from 1.7 to 3.1 and the LPRW varies from 590 to 730 nm. A linear relationship is obtained by fitting the LPRW with respect to the aspect ratio. This linear dependence is then utilized to determine the longitudinal plasmon energies of the nanorod monomers in each dimer on the basis of their measured sizes. The resulting data points are plotted in Figure 4d in terms of the plasmon energy. The red symbols represent the nanorods with a nearly fixed size. Their average longitudinal plasmon energy is 1.96 ± 0.02 eV. The blue symbols are for the nanorods of varying lengths. The plasmon energy varies from 1.85 to 2.32 eV. The coupled plasmon energies (green symbols) are red-shifted relative to the plasmon energies of both nanorod monomers and exhibit an anti-crossing-like behavior. This result indicates that the coupled plasmon energy can be desirably controlled by changing the plasmon energies of metal nanocrystal monomers even if the spacing between the nanocrystals is kept fixed. Because the plasmon shift resulting from the plasmon coupling as well as the electric field enhancement in the gap region is known to decay rapidly as the spacing is enlarged, our result will be useful for the optical applications where both large electric field enhancements and tunable plasmon energies are simultaneously required.

We last studied the effect of the end shape of elongated nanocrystals on the plasmon coupling because the electric field enhancement is known to be highly dependent on the nanocrystal curvature. Three types of elongated Au nanocrystals were prepared. They are nanorods, nanobipyramids, and nanobars. The nanorods are cylindrical in the middle segment and have rounded ends. Each nanobipyramid is composed of two pentagonal pyramids that are symmetrically and base-to-base stacked together. The ends are also rounded. The nanobars are rectangular and have clear facets at the ends. The measured average sizes of these nanocrystals are listed in Table 1. The dimers for all of the three types of Au nanocrystals were formed through the same dithiol (Figure S10, Supporting Information). Therefore, the gap spacing is approximately the same in all of the dimers.

The scattering properties of the dimers composed of the linearly end-to-end assembled nanocrystals were measured. Figure 5 shows the representative SEM images of the monomers, corresponding dimers, and their scattering spectra. The scattering peaks of the dimers are observed to be red-shifted considerably in comparison to those of the monomers. For each type of the elongated nanocrystals, the scattering spectral measurements were performed on about 5 monomers and 5 dimers. The resultant average scattering peak wavelengths are given in Table 1. The average LPRWs

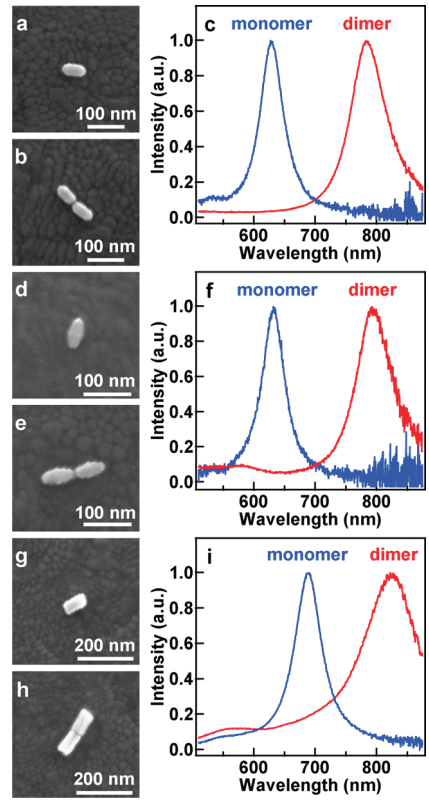

Figure 5. (a−c) SEM images and scattering spectra of a nanorod monomer and dimer. (d−f) SEM images and scattering spectra of a nanobipyramid monomer and dimer. (g−i) SEM images and scattering spectra of a nanobar monomer and dimer. The scattering spectra have been normalized.

of the nanorod and nanobipyramid monomers are both around 620 nm. Their coupled plasmon wavelengths are close to each other. Both are around 810 nm. The nanobars have an average LPRW of 690 nm. Their coupled plasmon is shifted to 850 nm. The coupling-induced plasmon shift for the nanobars is smaller than that for the nanorods and nanobipyramids in terms of wavelength. However, if the plasmon shift is converted from wavelength to energy, the fractional plasmon shifts in terms of energy for all of the three types of nanocrystals are nearly the same, around 20%, within the experimental error. We will carry out more experiments to further understand the shape effect on the plasmon coupling.

CONCLUSION

In summary, we have shown that the plasmon coupling in Au nanorod dimers that have similarly sized nanorods linked together at their ends with dithiol molecules gives the antibonding and bonding plasmon modes. The plasmon wavelengths of the two modes are observed to remain approximately unchanged, with the scattering intensity ratio between the two modes decaying rapidly as the angle between the nanorods is increased. The trend between the intensity ratio and nanorod angle has been corroborated by electrodynamic calculations, and a simple model based on the dipole−dipole interaction has been developed to understand the plasmon coupling properties in the nanorod dimers. The two plasmon modes are found to exhibit distinct electric field enhancement behaviors in the gap region. The electric field under the resonant excitation of the bonding mode is largely enhanced, while that for the antibonding mode is reduced in comparison to the far field. An anti-crossing-like behavior in the plasmon coupling energy diagram is revealed for linearly end-to-end assembled Au nanorod dimers composed of differently sized nanorods. The plasmon coupling properties between elongated Au nanocrystals of different shapes have further been studied. Our results will be of importance for a variety of plasmon-enhanced spectroscopies and for designing plasmonic circuits and optomechanic devices.

METHODS

Growth of the Au Nanorods. The Au nanorods were prepared using a seed-mediated method[38] together with anisotropic oxidation.[39,40] Specifically, the seed solution was made by injecting a freshly prepared, ice-cold aqueous $NaBH_4$ solution (0.01 M, 0.6 mL) into an aqueous mixture composed of $HAuCl_4$ (0.01 M, 0.25 mL) and cetyltrimethylammonium bromide (CTAB, 0.1 M, 9.75 mL), followed by rapid inversion mixing for 2 min. The resultant seed solution was kept at room temperature for more than 2 h before use. The growth solution was made by the sequential addition of aqueous $HAuCl_4$ (0.01 M, 2 mL), $AgNO_3$ (0.01 M, 0.4 mL), HCl (1.0 M, 0.8 mL), and ascorbic acid (0.1 M, 0.32 mL) solutions into an aqueous CTAB (0.1 M, 40 mL) solution. The resultant solution was mixed by swirling for 30 s. The seed solution was diluted by 10 times with deionized water, and 0.15 mL of the diluted seed solution was injected into the growth solution. The resultant reaction solution was gently mixed by inversion for 2 min and then left undisturbed overnight. The obtained nanorods, which had a LPRW of 740 nm, were then subjected to anisotropic oxidation by adding HCl (1.0 M, 0.2 mL) and H_2O_2 (30 wt %, 0.05 mL). The nanorod solution was kept in an isothermal oven at 65 °C to expedite the oxidation reaction. The oxidation process was monitored by measuring the extinction spectra of the nanorod solution from time to time. When the LPRW reached the desired value, the nanorods were washed by two cycles of centrifugation (4100*g*, 10 min) and redispersion in 0.1 M CTAB solutions to remove HCl.

Growth of the Au Nanobipyramids. The preparation of the Au nanobipyramids followed the procedure reported previously.[45] Briefly, the citrate-stabilized seed solution was obtained by adding a freshly prepared, ice-cold $NaBH_4$ solution (0.01 M, 0.15 mL) into an aqueous solution composed of $HAuCl_4$ (0.01 M, 0.125 mL), sodium citrate (0.01 M, 0.25 mL), and water (9.625 mL), followed by vigorous stirring. The resultant seed solution was kept at room temperature for 2 h before use. The growth solution was made by the sequential addition of $HAuCl_4$ (0.01 M, 1.2 mL), ascorbic acid (0.1 M, 0.402 mL), and $AgNO_3$ (0.01 M, 0.06 mL) solutions into an aqueous cetyltributylammonium bromide solution (0.01 M, 28.5 mL). Then, 0.15 mL of the seed solution was added to the growth solution, followed by gentle inversion mixing for 10 s. The resultant solution was kept undisturbed overnight in the isothermal oven at 65 °C. The as-grown Au nanobipyramids, which had a LPRW of 1000 nm, were then subjected to anisotropic oxidation to obtain nanobipyramids with desired LPRWs.

Growth of the Au Nanobars. A two-step seed-mediated method was utilized to prepare the Au nanobars.[46] Specifically, in the first step, the seed solution was prepared by adding a freshly prepared, ice-cold aqueous $NaBH_4$ solution (0.01 M, 0.6 mL) into an aqueous mixture composed of $HAuCl_4$ (0.01 M, 0.25 mL) and CTAB (0.1 M, 9.75 mL), followed by rapid inversion mixing for 2 min. The resultant seed solution was kept at room temperature for 2 h before use. The growth solution was made by the sequential addition of aqueous $HAuCl_4$ (0.01 M, 2.5 mL), $AgNO_3$ (0.01 M, 0.5 mL), and ascorbic acid (0.1 M, 0.275 mL) solutions into an aqueous CTAB solution (0.1 M, 47.5 mL). The resultant solution was mixed by swirling for 30 s. 0.06 mL of the seed solution was then added into the growth solution. The resultant solution was gently mixed by inversion for 2 min and then left undisturbed overnight. The nanorods obtained in this step had a LPRW of 827 nm. An isotropic overgrowth was conducted in the second step to produce the nanobars. Before the overgrowth, the nanorod solution obtained in the first step was concentrated by centrifugation (6300*g*) and redispersion in 10 mL of deionized water. The overgrowth solution was prepared by mixing aqueous $HAuCl_4$ (0.01 M, 0.28 mL), $AgNO_3$ (0.01 M, 0.025 mL), and CTAB (0.1 M, 11 mL) solutions together. HCl (1 M) was employed to adjust the pH value to ~4; then an ascorbic acid solution (0.01 M, 0.065 mL) was added. 0.2 mL of the concentrated nanorod solution was supplied, and the final mixture solution was kept at 30 °C overnight.

Formation of the Au Nanocrystal Dimers. The formation of the Au nanocrystal dimers was realized by first dispersing the nanocrystals in 1:4 (v/v) H_2O/CH_3CN mixture and then adding 1,8-octanedithiol as a linking molecule, according to the procedure described previously.[41] The particle concentrations of the Au nanocrystals are adjusted to be ~0.02 nM for the nanorods and nanobipyramids and ~0.01 nM for the nanobars according to their extinction coefficients.[38,40] The concentration of the dithiol was 1 μM. The assembly process in the mixture solvent was monitored by recording the time-dependent extinction spectra.

Instrumentation. Extinction spectral measurements were performed on a Hitachi U-3501 UV−visible/NIR spectrophotometer with 1 cm quartz cuvettes. SEM images were taken on an FEI Quanta 400 FEG microscope. Low-magnification TEM imaging

was performed on an FEI CM120 microscope at 120 kV. High-resolution TEM characterization was carried out on an FEI Tecnai F20 microscope. The Au nanocrystal dimers were deposited on ITO substrates by immersing the substrates in the solution for a controlled period of time and then blowing them dry with nitrogen. The nanocrystal monomers, dimers, and assemblies containing more than two nanocrystals were usually all observed on the substrates. The fraction of the dimers was maximized by controlling the elapsed time between the dithiol addition and substrate immersion, and the number density of the dimers was adjusted by varying the immersion time.

The scattering properties of the individual Au nanocrystal monomers and dimers were measured on a dark-field optical microscope (Olympus BX60) that was integrated with a quartz−tungsten−halogen lamp (100 W), a monochromator (Acton SpectraPro 2300i), and a charge-coupled device camera (Princeton Instruments Pixis 512B). The camera was thermoelectrically cooled to −70 °C during the measurements. A dark-field objective (100×, numerical aperture = 0.80) was employed for both illuminating the ITO substrate with the white excitation light and collecting the scattered light. The scattered light from the individual nanocrystal dimers were corrected by first subtracting the background spectra taken from the adjacent regions without Au nanocrystals and then dividing them with the calibrated response curve of the entire optical system.

FDTD Calculations. The FDTD calculations were performed using FDTD Solutions 6.0, which was developed by Lumerical Solutions, Inc. During the calculations, an electromagnetic pulse in the wavelength range from 500 to 900 nm was launched into a box containing the target Au nanostructure to simulate a propagating plane wave interacting with the nanostructure. The Au nanostructure and its surrounding space were divided into 0.5 nm meshes. The refractive index of the medium in the top and side regions was taken to be 1.0 and that in the bottom was set at 1.9 to simulate the ITO substrate. The Au nanorod was modeled as a cylinder capped with an oblate spheroid at each end. The diameter of the cylinder was 32 nm, and the length was 45 nm. The semimajor and semiminor axes of the spheroid were 16 and 10 nm, respectively. These sizes were very close to the measured average ones of the nanorod sample. For the dimer, the spacing between the nanorods at the closest point was set at 1.0 nm.

Acknowledgment. This work was supported by Hong Kong RGC GRF Grant No. CUHK403409, Project Code 2160391), NSFC/RGC Joint Research Scheme (No. N_HKU705/07), and NSFC (Project Code 20828001).

Supporting Information Available: Extinction spectra of the nanocrystal assembly, pattern-matching method, SEM images and scattering spectra of the nanorods before and after the thermal treatment, calculated and measured scattering spectra of the nanorod monomers, schematic showing the bonding and antibonding modes between the longitudinal and transverse plasmon modes, calculated scattering spectra of the dimers, electric field intensity enhancement profiles, plot of the intensity ratio *versus* the angle, coordinate system and derivation for the dipolar model, TEM and SEM images of the nanobipyramids and nanobars. This material is available free of charge *via* the Internet at http://pubs.acs.org.

REFERENCES AND NOTES

1. Shegai, T.; Li, Z. P.; Dadosh, T.; Zhang, Z. Y.; Xu, H. X.; Haran, G. Managing Light Polarization *via* Plasmon-Molecule Interactions within an Asymmetric Metal Nanoparticle Trimer. *Proc. Natl. Acad. Sci. U.S.A.* **2008**, *105*, 16448–16453.
2. Li, W. Y.; Camargo, P. H. C.; Lu, X. M.; Xia, Y. N. Dimers of Silver Nanospheres: Facile Synthesis and Their Use as Hot Spots for Surface-Enhanced Raman Scattering. *Nano Lett.* **2009**, *9*, 485–490.
3. Kim, S.; Jin, J.; Kim, Y.-J.; Park, I.-Y.; Kim, Y.; Kim, S.-W. High-Harmonic Generation by Resonant Plasmon Field Enhancement. *Nature* **2008**, *453*, 757–760.
4. Kinkhabwala, A.; Yu, Z. F.; Fan, S. H.; Avlasevich, Y.; Müllen, K.; Moerner, W. E. Large Single-Molecule Fluorescence Enhancements Produced by a Bowtie Nanoantenna. *Nat. Photonics* **2009**, *3*, 654–657.
5. Ueno, K.; Juodkazis, S.; Mizeikis, V.; Sasaki, K.; Misawa, H. Clusters of Closely Spaced Gold Nanoparticles as a Source of Two-Photon Photoluminescence at Visible Wavelengths. *Adv. Mater.* **2008**, *20*, 26–30.
6. Sundaramuethy, A.; Schuck, P. J.; Conley, N. R.; Fromm, D. P.; Kino, G. S.; Moerner, W. E. Toward Nanometer-Scale Optical Photolithography: Utilizing the Near-Field of Bowtie Optical Nanoantennas. *Nano Lett.* **2006**, *6*, 355–360.
7. Ueno, K.; Juodkazis, S.; Shibuya, T.; Yokota, Y.; Mizeikis, V.; Sasaki, K.; Misawa, H. Nanoparticle Plasmon-Assisted Two-Photon Polymerization Induced by Incoherent Excitation Source. *J. Am. Chem. Soc.* **2008**, *130*, 6928–6929.
8. Grigorenko, A. N.; Roberts, N. W.; Dickinson, M. R.; Zhang, Y. Nanometric Optical Tweezers Based on Nanostructured Substrates. *Nat. Photonics* **2008**, *2*, 365–370.
9. Mühlschlegel, P.; Eisler, H.-J.; Martin, O. J. F.; Hecht, B.; Pohl, D. W. Resonant Optical Antennas. *Science* **2005**, *308*, 1607–1609.
10. Schnell, M.; García-Etxarri, A.; Huber, A. J.; Crozier, K.; Aizpurua, J.; Hillenbrand, R. Controlling the Near-Field Oscillations of Loaded Plasmonic Nanoantennas. *Nat. Photonics* **2009**, *3*, 287–291.
11. Maier, S. A.; Kik, P. G.; Atwater, H. A.; Meltzer, S.; Harel, E.; Koel, B. E.; Requicha, A. A. G. Local Detection of Electromagnetic Energy Transport below the Diffraction Limit in Metal Nanoparticle Plasmon Waveguides. *Nat. Mater.* **2003**, *2*, 229–232.
12. Ozbay, E. Plasmonics: Merging Photonics and Electronics at Nanoscale Dimensions. *Science* **2006**, *311*, 189–193.
13. Rosi, N. L.; Mirkin, C. A. Nanostructures in Biodiagnostics. *Chem. Rev.* **2005**, *105*, 1547–1562.
14. Sannomiya, T.; Hafner, C.; Voros, J. *In Situ* Sensing of Single Binding Events by Localized Surface Plasmon Resonance. *Nano Lett.* **2008**, *8*, 3450–3455.
15. Ghosh, S. K.; Pal, T. Interparticle Coupling Effect on the Surface Plasmon Resonance of Gold Nanoparticles: From Theory to Applications. *Chem. Rev.* **2007**, *107*, 4797–4862.
16. Su, K.-H.; Wei, Q.-H.; Zhang, X.; Mock, J. J.; Smith, D. R.; Schultz, S. Interparticle Coupling Effects on Plasmon Resonances of Nanogold Particles. *Nano Lett.* **2003**, *3*, 1087–1090.
17. Nordlander, P.; Oubre, C.; Prodan, E.; Li, K.; Stockman, M. I. Plasmon Hybridization in Nanoparticle Dimers. *Nano Lett.* **2004**, *4*, 899–903.
18. Gunnarsson, L.; Rindzevicius, T.; Prikulis, J.; Kasemo, B.; Käll, M.; Zou, S. L.; Schatz, G. C. Confined Plasmons in Nanofabricated Single Silver Particle Pairs: Experimental Observations of Strong Interparticle Interactions. *J. Phys. Chem. B* **2005**, *109*, 1079–1087.
19. Khlebtsov, B.; Melnikov, A.; Zharov, V.; Khlebtsov, N. Absorption and Scattering of Light by a Dimer of Metal Nanospheres: Comparison of Dipole and Multipole Approaches. *Nanotechnology* **2006**, *17*, 1437–1445.
20. Jain, P. K.; El-Sayed, M. A. Surface Plasmon Coupling and Its Universal Size Scaling in Metal Nanostructures of Complex Geometry: Elongated Particle Pairs and Nanosphere Trimers. *J. Phys. Chem. C* **2008**, *112*, 4954–4960.
21. Tabor, C.; Murali, R.; Mahmoud, M.; El-Sayed, M. A. On the Use of Plasmonic Nanoparticle Pairs as a Plasmon Ruler: The Dependence of the Near-Field Dipole Plasmon Coupling on Nanoparticle Size and Shape. *J. Phys. Chem. A* **2009**, *113*, 1946–1953.
22. Shuford, K. L.; Meyer, K. A.; Li, C. C.; Cho, S. O.; Whitten, W. B.; Shaw, R. W. Computational and Experimental Evaluation of Nanoparticle Coupling. *J. Phys. Chem. A* **2009**, *113*, 4009–4014.
23. Chergui, M.; Melikyan, A.; Minassian, H. Calculation of Surface Plasmon Frequencies of Two, Three, and Four Strongly Interacting Nanospheres. *J. Phys. Chem. C* **2009**, *113*, 6463–6471.

24. Atay, T.; Song, J.-H.; Nurmikko, A. V. Strongly Interacting Plasmon Nanoparticle Pairs: From Dipole−Dipole Interaction to Conductively Coupled Regime. *Nano Lett.* **2004**, *4*, 1627–1631.
25. Jain, P. K.; Huang, W. Y.; El-Sayed, M. A. On the Universal Scaling Behavior of the Distance Decay of Plasmon Coupling in Metal Nanoparticle Pairs: A Plasmon Ruler Equation. *Nano Lett.* **2007**, *7*, 2080–2088.
26. Wang, H.; Halas, N. J. Plasmonic Nanoparticle Heterodimers in a Semiembedded Geometry Fabricated by Stepwise Upright Assembly. *Nano Lett.* **2006**, *6*, 2945–2948.
27. Lassiter, J. B.; Aizpurua, J.; Hernandez, L. I.; Brandl, D. W.; Romero, I.; Lal, S.; Hafner, J. H.; Nordlander, P.; Halas, N. J. Close Encounters between Two Nanoshells. *Nano Lett.* **2008**, *8*, 1212–1218.
28. Jain, P. K.; Eustis, S.; El-Sayed, M. A. Plasmon Coupling in Nanorod Assemblies: Optical Absorption, Discrete Dipole Approximation Simulation, and Exciton-Coupling Model. *J. Phys. Chem. B* **2006**, *110*, 18243–18253.
29. Willingham, B.; Brandl, D. W.; Nordlander, P. Plasmon Hybridization in Nanorod Dimers. *Appl. Phys. B: Laser Opt.* **2008**, *93*, 209–216.
30. Sun, Z. H.; Ni, W. H.; Yang, Z.; Kou, X. S.; Li, L.; Wang, J. F. pH-Controlled Reversible Assembly and Disassembly of Gold Nanorods. *Small* **2008**, *4*, 1287–1292.
31. Tabor, C.; Van Haute, D.; El-Sayed, M. A. Effect of Orientation on Plasmonic Coupling between Gold Nanorods. *ACS Nano* **2009**, *3*, 3670–3678.
32. Chu, M.-W.; Myroshnychenko, V.; Chen, C. H.; Deng, J.-P.; Mou, C.-Y.; García de Abajo, F. J. Probing Bright and Dark Surface-Plasmon Modes in Individual and Coupled Noble Metal Nanoparticles Using an Electron Beam. *Nano Lett.* **2009**, *9*, 399–404.
33. Funston, A. M.; Novo, C.; Davis, T. J.; Mulvaney, P. Plasmon Coupling of Gold Nanorods at Short Distances and in Different Geometries. *Nano Lett.* **2009**, *9*, 1651–1658.
34. Verellen, N.; Sonnefraud, Y.; Sobhani, H.; Hao, F.; Moshchalkov, V. V.; Dorpe, P. V.; Nordlander, P.; Maier, S. A. Fano Resonances in Individual Coherent Plasmonic Nanocavities. *Nano Lett.* **2009**, *9*, 1663–1667.
35. Reinhard, B. M.; Siu, M.; Agarwal, H.; Alivisatos, A. P.; Liphardt, J. Calibration of Dynamic Molecular Rulers Based on Plasmon Coupling between Gold Nanoparticles. *Nano Lett.* **2005**, *5*, 2246–2252.
36. Sönnichsen, C.; Reinhard, B. M.; Liphardt, J.; Alivisatos, A. P. A Molecular Ruler Based on Plasmon Coupling of Single Gold and Silver Nanoparticles. *Nat. Biotechnol.* **2005**, *23*, 741–745.
37. Reinhard, B. M.; Sheikholeslami, S.; Mastroianni, A.; Alivisatos, A. P.; Liphardt, J. Use of Plasmon Coupling to Reveal the Dynamics of DNA Bending and Cleavage by Single EcoRV Restriction Enzymes. *Proc. Natl. Acad. Sci. U.S.A.* **2007**, *104*, 2667–2672.
38. Ming, T.; Kou, X. S.; Chen, H. J.; Wang, T.; Tam, H.-L.; Cheah, K.-W.; Chen, J.-Y.; Wang, J. F. Ordered Gold Nanostructure Assemblies Formed By Droplet Evaporation. *Angew. Chem., Int. Ed.* **2008**, *47*, 9685–9690.
39. Tsung, C.-K.; Kou, X. S.; Shi, Q. H.; Zhang, J. P.; Yeung, M. H.; Wang, J. F.; Stucky, G. D. Selective Shortening of Single-Crystalline Gold Nanorods by Mild Oxidation. *J. Am. Chem. Soc.* **2006**, *128*, 5352–5353.
40. Ni, W. H.; Kou, X. S.; Yang, Z.; Wang, J. F. Tailoring Longitudinal Surface Plasmon Wavelengths, Scattering and Absorption Cross Sections of Gold Nanorods. *ACS Nano* **2008**, *2*, 677–686.
41. Pramod, P.; Thomas, K. G. Plasmon Coupling in Dimers of Au Nanorods. *Adv. Mater.* **2008**, *20*, 4300–4305.
42. Chen, H. J.; Sun, Z. H.; Ni, W. H.; Woo, K. C.; Lin, H.-Q.; Sun, L. D.; Yan, C. H.; Wang, J. F. Plasmon Coupling in Clusters Composed of Two-Dimensionally Ordered Gold Nanocubes. *Small* **2009**, *5*, 2111–2119.
43. Link, S.; El-Sayed, M. A. Spectral Properties and Relaxation Dynamics of Surface Plasmon Electronic Oscillations in Gold and Silver Nanodots and Nanorods. *J. Phys. Chem. B* **1999**, *103*, 8410–8426.
44. Gluodenis, M.; Foss, C. A. Jr. The Effect of Mutual Orientation on the Spectra of Metal Nanoparticle Rod−Rod and Rod−Sphere Pairs. *J. Phys. Chem. B* **2002**, *106*, 9484–9489.
45. Kou, X. S.; Ni, W. H.; Tsung, C.-K.; Chan, K.; Lin, H.-Q.; Stucky, G. D.; Wang, J. F. Growth of Gold Bipyramids with Improved Yield and Their Curvature-Directed Oxidation. *Small* **2007**, *3*, 2103–2113.
46. Sohn, K.; Kim, F.; Pradel, K. C.; Wu, J. S.; Peng, Y.; Zhou, F. M.; Huang, J. X. Construction of Evolutionary Tree for Morphological Engineering of Nanoparticles. *ACS Nano* **2009**, *3*, 2191–2198.